DOI: 10.13009/EUCASS2025-555
11TH EUROPEAN CONFERENCE FOR AERONAUTICS AND SPACE SCIENCES (EUCASS)

TOWARDS ROBUST ANGLES-ONLY RELATIVE ORBIT NAVIGATION: ASSESSING KEY MODELLING FACTORS USING BATCH LEAST SQUARES FILTERING

Alessandro Scalvini⋆†, *Giacomo Borelli*⋆ *and Gabriella Gaias*⋆
⋆*Politecnico di Milano*
Department of Aerospace Science and Technology, Politecnico di Milano, Via La Masa 34, 20156 Milano, Italy
alessandro.scalvini@polimi.it · giacomo.borelli@polimi.it · gabriella.gaias@polimi.it
†Corresponding author

Abstract

Autonomous operations demands for robust angles-only navigation algorithms that overcome weak observability. Batch least squares filtering, traditionally used for ground-based *post-facto* orbit determination, is now considered for computationally efficient space-borne applications. This approach may provide near real-time cross-checks for sequential filters or backup reinitialisation in case of divergence. A critical first step is to assess the performance influence of key filter components: modelling of propagation, manoeuvres and measurements as well as size and length of the batch processed by the filter. This study systematically examines these factors for angles-only relative orbit estimation to identify an optimal structure of the filter.

1. Introduction

Autonomous rendezvous and proximity operations are increasingly relevant in modern space missions, ranging from formation flying[1,2] to satellite servicing[3–5] and active debris removal.[3,6,7] Within this context, angles-only (AO) relative navigation has emerged as a viable solution for the far-to mid-range rendezvous with non-cooperative targets.[8,9] With this strategy, the relative motion of a target is estimated from line-of-sight (LoS) measurements, obtained via a vision-based sensor (VBS) suite. The main advantages include the use of passive cameras characterised by low power consumption, high dynamic range and low hardware cost. However, these benefits come at the cost of weak observability and more complex navigation algorithms and architectures.[8]

Traditionally, sequential filtering approaches such as the extended Kalman filter[10] or the unscented Kalman filter[11] have been successfully employed for state estimation in angles-only scenarios. These methods perform well in numerical simulation environments but in-flight campaigns shown that improper handling of few outliers may cause filter divergence.[12,13] To address these limitations, batch processing techniques, specifically batch least squares (LSQ) filtering, may offer a promising complementary solution. While batch filtering has traditionally been used for ground-based, *post-facto* relative orbit determination, interest is growing in computationally efficient reformulations applicable for space-borne implementations. Such an approach could provide a near real-time cross-check for sequential filters or serve as a backup for reinitialisation in case of filter divergence.[13]

A critical first step in this direction involves an extensive assessment of the performance influence of four key components of the estimation loop represented in Figure 1: propagation models, inclusion and modelling of manoeuvres and measurements prediction pipeline. Additionally, the filter design and performance are affected by the size and length of the batch of observations used to carry out the estimation. This work builds upon the foundational contributions to angles-only navigation presented by Gaias et al.[14] and aims at expanding the analysis conducted by Sullivan et al.[15] In the former, an on-ground LSQ-based navigation strategy based on relative orbital elements (ROEs) and a basic analytical propagation model including J_2 perturbations was presented. The authors[14] demonstrated that the inclusion of the J_2 perturbation in the propagation model leads to a (weakly) observable scenario, rather than a completely unobservable one, as in the unperturbed cased analysed in depth by Woffiden[16] and Lovell.[17] In fact, the algorithm proposed by Gaias et al.[14] was capable of successfully navigating the chaser satellite during a simulated rendezvous operation, despite the mentioned shortcomings due to low observability which were resolved by leveraging the manoeuvres performed during the approach to the target. However, the propagation method adopted in[14] lacked the modelling of the effect of non-vanishing relative semi-major axis,[18] accounted partially of the rotation of the eccentricity vector[19,20] and considered (only) J_2 effects to the first order.[19] Furthermore, the mapping from ROEs to LoS

DOI: 10.13009/EUCASS2025-555

was first order linear and lacked the correction to account for orbit curvature. All these facts result in low degree of observability that negatively impact the performance of the navigation. Nevertheless, the work[14] paved the way for the development of the onboard navigation system of the AVANTI experiment,[8] with proper enhancements to include the effect of differential aerodynamic drag.[18] In fact, the ground-based relative orbit determination described by Ardaens[21] employed numerical integration and full non-linear transformations in measurement modelling to achieve the best possible estimation accuracy. Since then, several efforts in the literature focused on improving the fundamental blocks of the relative navigation problem. The work of Sullivan[15] provides a comprehensive survey and comparison of many possible propagation models from the literature. Afterwards, with regard to ROE-based methods only, Koenig et al.[20] improved the handling of the eccentricity of the reference orbit and the rotation of the relative eccentricity vector, whereas[19] further improved accuracy by including contribution of all zonal elements and second-order effects of Keplerian and J_2 terms. As for the overall AO relative navigation, Sullivan studied how properly including non-linearity in the modelling (at all stages of the process) helps in addressing weak observability, also for non-controlled orbit arcs.[11] In[22] focus was given to develop analytical mappings from ROE to LoS improving accuracy at far-range.

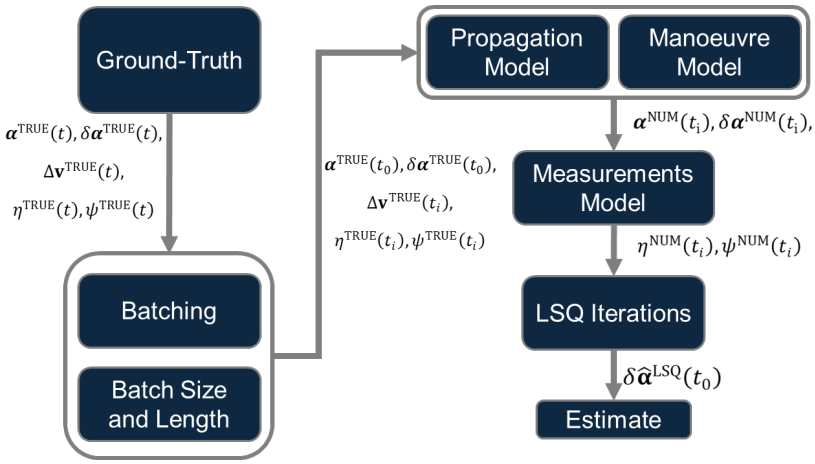

Figure 1: LSQ estimation pipeline and main components.

Consequently, this paper aims to complement the existing body of literature by systematically investigating how the fundamental modelling sub-blocks reported in Figure 1 influence the estimation. The four primary focus areas are: the *propagation models*, ranging from basic Keplerian dynamics to higher-fidelity analytical formulations that account for secular perturbations due to Earth non-spherical geo-potential; *manoeuvre modelling*, comparing instantaneous $\Delta\mathbf{v}$ impulses to continuous constant-thrust burn; *measurement modelling*, from first-order linear mappings that ignore orbital curvature to fully non-linear transformations; *batch size and length*, exploring configurations from short batches with sparse data to longer windows covering entire orbital periods with dense sampling. By conducting a sensitivity analysis across these dimensions, this study seeks to identify optimal combinations that grants the highest level of accuracy while maintaining analytical propagation, which is necessary to achieve efficient implementations. The investigation is carried out in a realistic simulation environment that mimics Low Earth Orbit (LEO) conditions inspired by the PRISMA[1] mission, incorporating perturbative effects such as Earth oblateness and moderate differential drag. Synthetic ground-truth trajectories are generated using a dedicated numerical propagator. The outcomes of this study are expected to provide valuable guidelines for the implementation of robust, angles-only navigation systems, whether for autonomous space-borne applications or semi-autonomous ground-based operations. Moreover, the analysis establishes a foundation for further research, including real-time implementation and hybrid approaches combining batch and sequential estimation.

The remainder of this paper is structured as follows. Section 2 introduces the theoretical background of propagation, manoeuvres and measurements models and reviews the formulation of the LSQ filtering technique. Section 3 details the methodology used for the sensitivity analysis, including the definitions of metrics for propagation accuracy (without and with manoeuvres), LoS mapping precision and estimation accuracy. In Section 4, simulation results are presented and discussed for a representative near-circular LEO scenario. Finally, Section 5 summarise the key findings of the study and presents the concluding remarks.

DOI: 10.13009/EUCASS2025-555

2. Theoretical Background

This section outlines the mathematical foundations of all sub-components of the filtering pipeline depicted in Figure 1, extensively from key references by Montenbruck et al.,[23] D'Amico et al.,[1] Gaias et al.,[14] and Sullivan et al.[11]

2.1 Manoeuvre-Free Propagation Modelling

Relative orbital elements constitute a convenient parametrisation for describing the relative motion of a deputy satellite with respect to a chief satellite since they are formulated as a combination of their absolute orbital elements.[11] In particular, the quasi-non-singular formulation[20] of the ROEs is used in this work. Let a, e, i, Ω, ω and M denote the classical Keplerian elements and $u = \omega + M$ the mean argument of latitude. By indicating with the subscripts C and D the quantities referring to the chief and deputy satellite, the dimensionless quasi-non-singular ROEs are defined as:

$$\delta\boldsymbol{\alpha} = \begin{pmatrix} \delta a \\ \delta\lambda \\ \delta e_x \\ \delta e_y \\ \delta i_x \\ \delta i_y \end{pmatrix} = \begin{pmatrix} (a_D - a_C)/a_C \\ u_D - u_C + (\Omega_D - \Omega_C)\cos(i_C) \\ e_D\cos(\omega_D) - e_C\cos(\omega_C) \\ e_D\sin(\omega_D) - e_C\sin(\omega_C) \\ i_D - i_C \\ (\Omega_D - \Omega_C)\sin(i_C) \end{pmatrix}, \tag{1}$$

where δa is the relative semimajor-axis, $\delta\lambda$ is the mean relative longitude, $(\delta e_x, \delta e_y)$ are the components of the relative eccentricity vector $\delta\mathbf{e}$ and $(\delta i_x, \delta i_y)$ are the components of the relative inclination vector $\delta\mathbf{i}$. Consider the Radial-Transversal-Normal (RTN) frame centred on the chief spacecraft. This local coordinate system has the Radial axis ($\hat{\mathbf{R}}$) pointing from the central body toward the chief, the Normal axis ($\hat{\mathbf{N}}$) aligned with the orbital angular momentum and the Transversal ($\hat{\mathbf{T}}$) axis lying in the orbital plane completing the right-handed triad. For a near-circular orbit, the geometric interpretation of the ROEs can be easily understood by projecting the relative motion onto the TR-plane and NT-plane, see for instance Figure 4.10 of Sullivan.[11] The radial and along-track relative motion are characterised by mean offsets given by $a\delta a$ and $a\delta\lambda$, respectively. The in-plane oscillatory motion traces out a 2:1 ellipse scaled by the magnitude of $a\delta\mathbf{e}$. The cross-track oscillatory motion, which has no mean offset, is instead scaled by the magnitude of the inclination vector $a\delta\mathbf{i}$. Besides providing an intuitive and geometrically meaningful representation of relative motion, a ROE-based formulation offers several advantages over traditional Cartesian (position-velocity) formulations. It enables direct constraint enforcement of collision avoidance and formation flying[1] constraints and allows to straightforwardly account for the effect of perturbations.[20] In particular, it is possible to retain these effects in analytical formulations of the state transition matrix (STM).[8,20] In this work the use of the following orbital elements based propagation methods are compared: HCW-STM for pure Keplerian motion, GDA-STM[14] that includes the secular J_2 effect with some simplifications (*i.e.*, approximation on the rotation of the relative eccentricity vector), GA-STM[24] that uses OE-differences and is applicable to also eccentric case, and GCL-STM[19] that includes effect of all zonal terms of the geo-potential and provides the second-order expansion (state transition tensor STT) for Keplerian an J_2 contributions for arbitrary eccentricity of the reference orbit. Note that GA-STM and the STM of[20] are equivalent to the net of adopting a different parametrisation. Moreover, all the STM including geo-potential perturbations require proper transformations to retrieve the mean orbital elements. Ref[14] and[24] use a first-order transformation, whereas GCL-STM adopts an analytical solution accurate to the second-order in J_2 (limited to the near-circular case).

Table 1: Analytical propagation models

Model	Orbit Type	Perturbations	Solution Form
HCW-STM	$e \approx 0$	None	STM
GDA-STM[14]	$e \approx 0$	J_2	STM
GA-STM[24]	$0 \leq e < 1$	J_2	STM
GCL-STM[19]	$0 \leq e < 1$	J_2, J_4, J_6	STM, STT

We restrict the numerical comparison to near-circular applications in LEO. In this scenario the superposition of the effects can be employed[18] to separate the effects of the different perturbations included. For a scenario subject to only the J_2 perturbation, we can write the ROE evolution as in:[18]

$$\delta\boldsymbol{\alpha}(t) = \boldsymbol{\Phi}(t, t_0)\delta\boldsymbol{\alpha}_0 = \left(\boldsymbol{\Phi}_{\mathrm{HCW}}(t, t_0) + \boldsymbol{\Phi}_{J_2}(t, t_0)\right)\delta\boldsymbol{\alpha}_0, \tag{2}$$

where t is a generic time instant and t_0 the initial time. The STMs in the previous are reported and explained in.[14,18–20,24]

DOI: 10.13009/EUCASS2025-555

Notice that relative motion model of Equations (2) is fully linear in the initial relative state $\delta\boldsymbol{\alpha}_0$. Moreover, it is possible to distinguish the effects on the evolution of $\delta\boldsymbol{\alpha}(t)$ due to Keplerian motion ($\boldsymbol{\Phi}_{\mathrm{HCW}}$) from the secular effects due J_2 ($\boldsymbol{\Phi}_{J_2}$). The inclusion of the J_2 perturbation results in two main effects: the secular drift of in the mean relative longitude $\delta\lambda$ and in the y component of the relative inclination vector (δi_y) and the rotation of the relative eccentricity vector $\delta\mathbf{e}$ with constant rate. Neglecting these effects leads to non-negligible propagation error, unobservability and possibly to unsafe operations. For further details on the analytical propagation of the relative motion and on the effects of perturbations, the reader is encouraged to refer to.[11,14,15,18–20,24] To achieve accurate state propagation, it is essential to consider the time evolution of the chief satellite mean absolute orbital elements (OE), denoted as $\boldsymbol{\alpha}_C(t)$. It is assumed that estimates of $\boldsymbol{\alpha}_C(t)$ are available at discrete time intervals, for example, from a GNSS-based navigation filter. However, these estimates may not be synchronised with the timestamps of the VBS measurements or with the execution time of manoeuvres. As a result, it becomes necessary to interpolate or propagate the absolute state to the desired time instants. In this study, the initial mean orbital elements $\boldsymbol{\alpha}_C(t_0)$ are analytically propagated to the measurement or manoeuvre time using a satellite dynamics model consistent with the one adopted for the relative motion. For instance, if the ROEs are propagated under Keplerian dynamics, then the chief mean OEs are also propagated under the same assumption. This consistency is maintained for higher-fidelity models that include perturbative forces. A critical factor for accurate propagation lies in the accuracy of the initial conditions, namely the mean ROEs and the chief mean OEs, $(\delta\boldsymbol{\alpha}(t_0), \boldsymbol{\alpha}_C(t_0))$. These are derived from their osculating counterparts at the initial time (taken from the ground truth) via an osculating-to-mean transformation. Although different dynamical models may be based on distinct assumptions, the same transformation is applied to initialise all analytical propagations. This transformation introduces corrections for the J_2 effect, slightly improving the performance of simplified models such as the HCW-STM, which do not account for perturbations. However, the results demonstrate that this improvement remains marginal.

2.2 Manoeuvre Modelling

In the previous section, the analytical propagation of the unforced evolution of the ROEs using STMs was discussed. However, on-orbit operations typically involve active manoeuvres, which must be incorporated into the dynamic propagation. By linearising the non-linear equations of relative motion about the chief orbit[1,8] it is possible to find a closed from solution to propagate the initial ROEs considering both the unforced motion and the effects of manoeuvres:

$$\delta\boldsymbol{\alpha}(t) = \boldsymbol{\Phi}(t_0, t)\delta\boldsymbol{\alpha}_0 + \int_{t_0}^{t} \boldsymbol{\Phi}(t_0, \tau)\mathbf{B}(\tau)^R\mathbf{u}_c(\tau)d\tau, \tag{3}$$

where ${}^R\mathbf{u}_c(t)$ is a generic control profile and $\mathbf{B}(t)$ is the time-variant input sensitivity matrix that maps the control input into ROE-space. The superscript "R" indicates that the quantity is expressed in the RTN frame. The above equation is thus composed by a zero-input response and a zero-state response. The latter component is obtained by solving the definite integral, which can be done analytically or numerically by means of some discretisation. A particularly simple case is obtained when a manoeuvre can be considered impulsive and the instantaneous "jump" in ROEs reduces to:

$$\Delta(\delta\boldsymbol{\alpha}(t_{\mathrm{M}})) = \mathbf{B}(t_{\mathrm{M}})\,{}^R\Delta\mathbf{v}(t_{\mathrm{M}}), \tag{4}$$

where $\mathbf{B}(t_{\mathrm{M}})$ is the input matrix evaluated at the time of the manoeuvre, t_{M}, or equivalently at the mean argument of latitude $u_C(t_{\mathrm{M}})$ at which the chief executes the manoeuvre. This matrix is derived from the Gauss variational equations, as detailed in.[1] Throughout this work, it is implicitly assumed that manoeuvres applied to the mean orbit produce equivalent effects as those applied to the true (osculating) orbit. Therefore, $u_C(t_{\mathrm{M}})$ is interpreted as the mean argument of (mean) latitude at the time of the manoeuvre. Sometimes, the manoeuvres performed during the operation have duration comparable to the chief orbit period, making the assumption leading to Equation (4) inadequate. We still assume the manoeuvre has a constant thrust or, at least, that can be divided into constant-thrust segments. With this in mind, it could be possible to follow the work of Grzymisch et al.[25] to analytically solve the integral in Equation (3). While this approach leads to a fast implementation (analytical solution) and would likely be the correct choice for the flight software, it requires to solve the integral for each different propagation model considered in this analysis, reported in Table 1. For simplicity, in this work it is decided to approximate a continuous manoeuvre with a set of equivalent impulses. The decomposition of a continuous manoeuvres into impulses is obtained with the following steps:

1. Compute the number of impulses as

$$n_{\mathrm{IMP}} = \mathrm{ceil}\left(\frac{\Delta t_{\mathrm{M}}}{\Delta t_{\mathrm{MAX}}}\right),$$

where $\Delta t_{\mathrm{M}} = t_{\mathrm{M}}^{\mathrm{END}} - t_{\mathrm{M}}^{\mathrm{START}}$ is the duration of the manoeuvre and Δt_{MAX} is the user-selected threshold length to assume impulsive manoeuvre. The function "ceil" rounds the ratio to an integer value.

DOI: 10.13009/EUCASS2025-555

2. Divide the continuous manoeuvre in n_{IMP} segments of same duration Δt_{MAX}. For each of the segment we can compute the equivalent impulsive manoeuvre as:

$$\Delta \mathbf{v}_i = \frac{\mathbf{F}}{m} \Delta t_{\text{MAX}}$$

Given that the original manoeuvre is constant, the thrust $\mathbf{F}$ is the same across each segment and the mass m of the spacecraft is assumed to remain unvaried. The equivalent set of impulsive manoeuvre is thus obtained.

3. Each manoeuvre of the set is then introduced in the propagation using Equations (4). To increase the precision of discretisation, each impulse $\Delta \mathbf{v}_i$ is applied at the midpoint of the corresponding segment. Between two consecutive midpoints the dynamics is unforced, thus the ROEs are propagated as discussed in Section 2.1.

During the formation flying operations, the manoeuvres are usually quite small (from mm/s to few cm/s) and in general the chief (the manoeuvring spacecraft) orbit is not affected much by the them. However, for the sake of consistency, also the mean OE of the chief are updated with the same strategy outlined in this section but applied to the mean OEs of the chief instead of the ROEs. In particular, the input sensitivity matrix to map the ${}^{R}\Delta\mathbf{v}(t_{\text{M}})$ to the change in $\boldsymbol{\alpha}_C$ is obtained from the Gauss Variational Equations reported in Vallado.[26]

2.3 Measurement Modelling

Coherently with the work of Gaias et al.,[14] the AO observation at each time instant consist of two angles: the azimuth η and elevation ψ. These angles subtend the LoS unit vector pointing from the centre-of-mass (CoM) of the chief to the one of the deputy and is expressed in the VBS frame:

$${}^{V}\mathbf{u} = \frac{{}^{V}\mathbf{r}}{||\mathbf{r}||}, \tag{5}$$

Assuming that this frame origin coincided with the chief CoM and assuming that the bore-sight points in the anti-flight direction, it is possible to obtain the rotation matrix from RTN to VBS frame (${}^{V}\mathbf{R}_R$) as in.[14,22] This rotates the position vector ${}^{R}\mathbf{r}$, which corresponds to the position component of the relative state expressed in RTN frame (${}^{R}\delta\mathbf{x}$), into the VBS frame. Consequently, the measurements vector composed by azimuth and elevation is defined as follows:

$$\mathbf{z}(t, \boldsymbol{\alpha}_C(t), \delta\boldsymbol{\alpha}(t)) = \begin{pmatrix} \eta \\ \psi \end{pmatrix} = \begin{pmatrix} \arctan({}^{V}u_x / {}^{V}u_z) \\ \arcsin({}^{V}u_y) \end{pmatrix} \tag{6}$$

What remains to be discussed is the process to obtain the relative state expressed in RTN frame (${}^{R}\delta\mathbf{x}$) from the ROEs (and the mean absolute OE of the chief). The simplest way to achieve this would be to use a simple (but inaccurate) direct linear mapping from $\delta\boldsymbol{\alpha}$ to ${}^{R}\delta\mathbf{x}$ as described in.[14] Alternatively, it is possible to follow the more structured pipeline presented in.[11]Regardless of the strategy, the first three components of ${}^{R}\delta\mathbf{x}$ are the relative position vector ${}^{R}\mathbf{r}$ that can be normalised and rotated to the VBS-frame to obtain the LoS vector ${}^{R}\mathbf{u}$ using Equations (5). Consequently the azimuth and elevation angles are immediately obtained from Equation (6). In this work several LoS mapping summarised in Table 2 are compared.

Table 2: Mapping to LoS models

Model	Mapping Type	Orbit Curvature	Orbit Curvature Strategy
GDA-MAP[14]	First-order linear	No	N/A
GA-MAP-r[24]	First-order linear	No	N/A
GA-MAP-c[24]	First-order linear	Yes	Curvilinear to rectilinear transformation
GAC-MAP[22]	Non-linear	Yes	Numerical solution of Kepler's equation

Independently of the chosen mapping, we must always apply a mean-to-osculating transformation to ROEs and OEs before computing the LoS. This is essential since mean elements are a mathematical abstractions used for computational simplicity, while the osculating orbital elements represent the actual, instantaneous orbit. Since the filter compares sensor measurements, taken in the real, osculating environment, with an on-board model, consistency is crucial. Both must refer to osculating quantities to ensure coherence between model predictions and real-world observations.

DOI: 10.13009/EUCASS2025-555

2.4 Batch LSQ Filtering Framework

In this work the relative orbit estimation problem is solved via a least-square methodology. In particular, we seek the estimate of the initial state $\delta\hat{\boldsymbol{\alpha}}_0^{\text{LSQ}}$ that minimises the weighted squared sum of the difference between the actual measurements and the ones predicted using the current estimate $\delta\hat{\boldsymbol{\alpha}}_0$ propagated to the generic time instant t:

$$\boldsymbol{\rho}(t, \delta\hat{\boldsymbol{\alpha}}_0) = \mathbf{z}(t, \boldsymbol{\alpha}_C(t), \delta\hat{\boldsymbol{\alpha}}(t)) - \mathbf{z}^{\text{TRUE}}(t) \tag{7}$$

The measurements vector $\mathbf{z}^{\text{TRUE}}(t)$ is obtained either from the real data or from the ground truth simulator. The quantity $\mathbf{z}(t, \boldsymbol{\alpha}_C(t), \delta\hat{\boldsymbol{\alpha}})$ is instead computed within the filter by propagating the current estimate $\delta\hat{\boldsymbol{\alpha}}_0$ to the time instant t (at which the observation is conducted) as described in Sections 2.1 and 2.2. By now considering a finite batch of measurements containing $|B|$ data-points, it is possible to define the column array of stacked residuals as:

$$\boldsymbol{\rho}(\delta\hat{\boldsymbol{\alpha}}_0) = \left(\boldsymbol{\rho}_1{}^{\top}(t_0, \delta\hat{\boldsymbol{\alpha}}_0), \cdots, \boldsymbol{\rho}_i{}^{\top}(t_i, \delta\hat{\boldsymbol{\alpha}}_0), \cdots, \boldsymbol{\rho}_{|B|}{}^{\top}(t_{|B|}, \delta\hat{\boldsymbol{\alpha}}_0)\right)^{\top} \tag{8}$$

The subscript i indicates that the residual vector is referred to the i-th time instant (i-th data point of the batch). Usually in (relative) orbit determination and navigation problem, a coarse a-priori value of the quantity being estimated is available (from Two-Line-Elements or initial relative orbit determination) alongside with measure of the uncertainty associated to it. In particular we assume to know the a-priori estimate of the initial ROEs $\delta\hat{\boldsymbol{\alpha}}_0^{\text{APR}}$ and the associated a-priori covariance $\mathbf{P}_0^{\text{APR}}$. By following the work of Montenbruck et al.,[23] it is possible to formulate the cost functional to be minimised as follows:

$$J = \left(\delta\hat{\boldsymbol{\alpha}}_0 - \delta\hat{\boldsymbol{\alpha}}_0^{\text{APR}}\right)^{\top} \boldsymbol{\Lambda}^{\text{APR}} \left(\delta\hat{\boldsymbol{\alpha}}_0 - \delta\hat{\boldsymbol{\alpha}}_0^{\text{APR}}\right) + \boldsymbol{\rho}(\delta\hat{\boldsymbol{\alpha}}_0)^{\top}\mathbf{W}\boldsymbol{\rho}(\delta\hat{\boldsymbol{\alpha}}_0).$$

Where $\boldsymbol{\Lambda}^{\text{APR}} = \left(\mathbf{P}_0^{\text{APR}}\right)^{-1}$ is the a-priori information matrix and $\mathbf{W} = \text{blkdiag}\left(\mathbf{W}_1, \cdots, \mathbf{W}_{|B|}\right)$ is a block diagonal weighting matrix composed by the covariance matrices of the measurement: $\mathbf{W}_i = \text{diag}\left(\frac{1}{\sigma_{\eta,i}^2}, \frac{1}{\sigma_{\psi,i}^2}\right)$. The quantities at denominator are the variances of the azimuth and elevation measurements errors and depend on the sensor (model) and operating conditions. Coherently with the work of Gaias et al.,[14] it also necessary to define the matrix of accumulated partials of the measurements with respect to the initial state:

$$\mathbf{H} = \left(\left[\mathbf{C}(t_0)\boldsymbol{\Phi}(t_0, t_0)\right]^{\top}, \cdots, \left[\mathbf{C}(t_i)\boldsymbol{\Phi}(t_0, t_i)\right]^{\top}, \cdots, \left[\mathbf{C}(t_{|B|})\boldsymbol{\Phi}(t_0, t_{|B|})\right]^{\top}\right)^{\top}. \tag{9}$$

Where $\mathbf{C}(t_i)$ is the measurements sensitivity matrix[11,14] evaluated at the time instant t_i. This last quantity is the Jacobian of the measurements (Equation (6)) with respect to the relative state vector $\delta\boldsymbol{\alpha}$. This quantity can be derived analytically for a selected measurements model but, since in this work several different models are considered, it is computed numerically. The final implementation of the filter should however use the analytical form to benefit computational efficiency. Finally, the local minimum (found in the proximity of the a-priori estimate) that best fits the observations in a least-square of the residuals sense is given by the iterations:

$$\begin{aligned} \mathbf{P}_0^{[j+1]} &= \left(\boldsymbol{\Lambda}^{\text{APR}} + \mathbf{H}^{[j]\top}\mathbf{W}^{-1}\mathbf{H}^{[j]}\right)^{-1} \\ \delta\hat{\boldsymbol{\alpha}}_0^{[j+1]} &= \delta\hat{\boldsymbol{\alpha}}_0^{[j]} + \mathbf{P}_0^{[j+1]}\left[\boldsymbol{\Lambda}^{\text{APR}}\left(\delta\hat{\boldsymbol{\alpha}}_0^{[j]} - \delta\hat{\boldsymbol{\alpha}}_0^{\text{APR}}\right) - \mathbf{H}^{[j]\top}\mathbf{W}^{-1}\boldsymbol{\rho}^{[j]}\right], \end{aligned} \tag{10}$$

starting from $j = 0$ and repeating until convergence is achieved. The output of the estimation being the LSQ estimate $\delta\hat{\boldsymbol{\alpha}}_0^{\text{LSQ}}$ and the associated covariance $\mathbf{P}_0^{\text{LSQ}}$.

3. Sensitivity Analysis

In order to determine the optimal configuration of the estimation pipeline components illustrated in Figure 1, this work adopts a sequential, greedy-like strategy, in which each sub-block is assessed independently. The underlying hypothesis is that a filter composed of the most accurate propagation model, the most effective manoeuvre modelling, and the most precise LoS mapping yields the highest estimation accuracy and filter robustness. Moreover, the chosen propagation models are limited to analytical formulations to limit the computational burden, thereby supporting the feasibility of space-borne implementation. The remainder of the section explains the performance assessment strategy and the metrics employed to quantify performance of each sub-component.

DOI: 10.13009/EUCASS2025-555

3.1 Metrics Definition for Propagation Accuracy

To evaluate the accuracy of the considered propagation models of Table 1, it is necessary to define meaningful simulation scenarios and metrics. To ensure a meaningful comparison, scenarios where the non-homogeneous mass distribution of the Earth is the main perturbation effect have been employed. In order to provide a quantitative measure of the accuracy of each model, the same metric employed in Sullivan[15] is used in this analysis since it provides a concise (scalar), easy-to-compute and meaningful error metric. For the sake of completeness, the definition is here reported:

$$\begin{aligned} \nu &= \max_{t_i} \|\mathbf{W}\left(\delta\mathbf{x}^{\mathrm{STM}}(t_i) - \delta\mathbf{x}^{\mathrm{TRUE}}(t_i)\right)\|_2 \text{ for } t_i = [t_0, t_F] \\ \mathbf{W} &= \mathrm{diag}\left(1, 1, 1,\ {n_C}^{-1}, {n_C}^{-1}, {n_C}^{-1}\right), \end{aligned} \tag{11}$$

where the superscript "TRUE" stands for the output of the ground-truth numerical simulator and the relative state $\delta\mathbf{x}^{\mathrm{TRUE}}(t_i)$ is obtained by rigorously transforming the numerically propagated inertial state of chief and deputy to Cartesian relative state expressed in the RTN frame of the chief.[15] The relative state $\delta\mathbf{x}^{\mathrm{STM}}(t_i)$ is instead obtained using the analytical propagation model under analysis. Then, the result is mapped to the Cartesian state using the highly precise, fully-non-linear transformation presented in Gaias et. al.[22] As we will demonstrate later in this work, this last is the most accurate among the mappings considered in Table 2, thus introducing negligible error in the analysis. The weighting matrix $\mathbf{W}$ is used to convert the velocity part of the state into a length by normalising it using the mean motion of the chief orbit n_C. Notice that the maximum norm of the (weighted) relative state error is computed across the simulation time to obtain the scalar metric ν for each model.

3.2 Metrics Definition for Manoeuvres Accuracy

Once the optimal propagation model has been identified, the next step is to assess how its accuracy is affected by the inclusion of manoeuvres during operations. In particular, it is crucial to determine under what conditions the assumption of an impulsive manoeuvre is valid, and when a continuous thrust model must be used instead. A straightforward way to quantify the modelling error introduced by these assumptions is to reuse the accuracy metric previously defined in Equation (11), as we are still evaluating propagation performance, now in the presence of a single manoeuvre. In all cases the manoeuvre is implemented as a continuous thrust in the simulator used to generate the ground truth (*i.e.*, $\delta\mathbf{x}^{\mathrm{TRUE}}(t_i)$). The best-performing propagation model is then paired with either an impulsive or continuous manoeuvre model to propagate the relative motion analytically. This process is carried out (as outlined in Section 2) twice, once assuming an impulsive manoeuvre and once assuming a continuous one, and the metric of Equation (11) is computed for both cases for comparison.

3.3 Metrics Definition for Measurements Accuracy

In Section 2.1, we described the pipeline that maps the ROEs, together with the chief absolute orbital elements, to the LoS vector and then computes the azimuth and elevation angles in the VBS frame. Specifically, this work considers the four mapping models listed in Table 2. Consistent with the approach of the previous section, we seek to define error metrics that are concise enough to allow efficient computation and visualisation across multiple scenarios, while also providing meaningful insights into the accuracy of each mapping model. With this goal in mind, a scalar metric to represent the angular error in the mapping from $\delta\boldsymbol{\alpha}$ (and $\boldsymbol{\alpha}_C$) to ${}^R\delta\mathbf{r}$ is defined as:

$$\theta = \max_{t_i} \left(\arccos\left(\frac{{}^R\delta\mathbf{r}^{\mathrm{MAP}}(t_i) \cdot {}^R\delta\mathbf{r}^{\mathrm{TRUE}}(t_i)}{\|{}^R\delta\mathbf{r}^{\mathrm{MAP}}(t_i) \cdot {}^R\delta\mathbf{r}^{\mathrm{TRUE}}(t_i)\|_2} \right) \right) \tag{12}$$

The angular metric is thus defined as the maximum angular error (across all time instants) formed by the ground truth position vector (superscript "TRUE") and the one obtained via mapping (superscript "MAP"). Notice that, depending on the mapping, the position vector ${}^R\delta\mathbf{r}^{\mathrm{MAP}}$ is directly[14] obtained or is extracted from the first three components[22] of ${}^R\delta\mathbf{x}^{\mathrm{MAP}}$. The angular error defined in Equation (12) provides a useful measure of mapping accuracy, but it is not sufficient on its own. A mapping may closely match the direction of the true LoS, resulting in a small value of θ, while still introducing a significant error in magnitude. To better discriminate between models, this metric is complemented by an additional measure related to the magnitude, defined as follows:

$$\begin{aligned} \gamma &= \max_{t_i} \left(\|\delta\mathbf{r}_{\|}{}^{\mathrm{MAP}}(t_i) - \delta\mathbf{r}^{\mathrm{TRUE}}(t_i)\|_2 \right) \\ \delta\mathbf{r}_{\|}{}^{\mathrm{MAP}}(t_i) &= \left(\frac{{}^R\delta\mathbf{r}^{\mathrm{MAP}}(t_i) \cdot {}^R\delta\mathbf{r}^{\mathrm{TRUE}}(t_i)}{{}^R\delta\mathbf{r}^{\mathrm{TRUE}}(t_i) \cdot {}^R\delta\mathbf{r}^{\mathrm{TRUE}}(t_i)} \right) \delta\mathbf{r}^{\mathrm{TRUE}}(t_i) \end{aligned} \tag{13}$$

DOI: 10.13009/EUCASS2025-555

This quantity is the maximum magnitude error measured in the direction of the true LoS. It is obtained by projecting the relative position obtained through a mapping onto the true LoS and then subtracting from it the true value. Combining the two metric of previous equations, it is possible to obtain a complete picture of the accuracy of the mapping.

3.4 Metrics Definition for Optimal Batch Size/Length

In previous sections, the metrics used to analyse the propagation (both with and without manoeuvres) and the accuracy of measurements have been addressed. Now, the focus shifts to studying the impact of two fundamental parameters of a batch least-squares (LSQ) filter: the batch *size* and *length*, defined as follows:

- **Batch Size** $|B|$: the number of data-points grouped in the batch. Each data-point includes its time instant, a tuple of (azimuth, elevation) angles, the absolute orbit and attitude of the chief spacecraft, the manoeuvres and other relevant quantities. We assume strict synchrony across all data-points, so every quantity in a data-point refers to the same time stamp.

- **Batch Length** Δt_B: the elapsed time between the first and last observations in the batch. This interval determines the temporal span over which the measurements are acquired.

The first parameter is important since it directly relates to the computational feasibility of the procedure. Recalling Equation (10), it is evident that the computational time scales with size of the batch size (each element adds a block row to matrix $\mathbf{H}$). The batch length instead relates both to propagation accuracy and operational difficulties.[13] In particular, longer propagation times are expected to result in greater propagation errors due to approximations and unmodeled dynamics, which progressively degrade the accuracy of the estimation process. On the other hand, a too-small Δt_B might not contain enough information about the relative motion to allow the estimation process. This problems might verify when the illumination is such that measurements can be taken only during a small portion of the chief orbit.

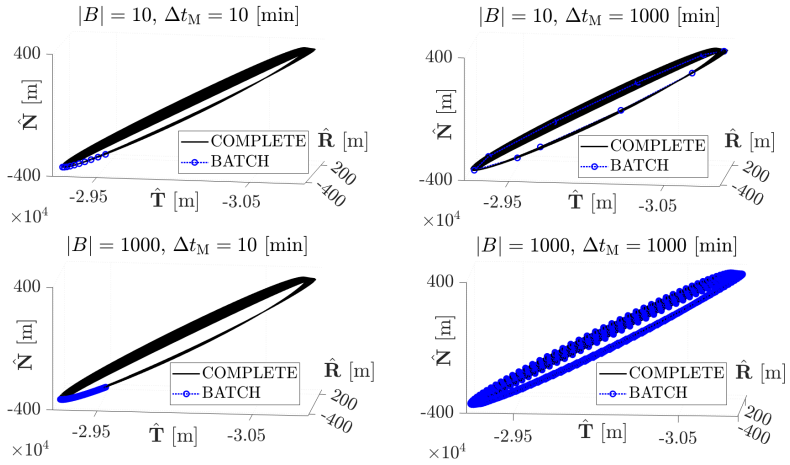

Figure 2: Visualisation of different batch sizes and lengths.

A visualisation of these parameters is presented in Figure 2 where the same relative orbit (black solid line) is sampled using four different combinations of $|B|$ and Δt_B to generate the batch data-points (blue circles). Notice that each data point, graphically depicted a relative position in RTN frame, contains all the quantities needed to estimate the orbit and evaluate the performance metrics.

The core objective of this analysis is to determine, for a given measurement interval (batch length), the minimum number of observations (batch size) required to achieve an accurate estimate of deputy relative orbit. To isolate the effects of the two parameters, a batch LSQ filter is constructed using the most accurate analytical propagation model in combination with the most precise fully non-linear LoS model. This combination is selected in accordance with the greedy-approach strategy described previously. With this goal in mind, the first performance metric considers the residuals between the predicted and true azimuth and elevation measurements. Following the approach introduced by Gaias et al.,[14] the quality of the estimate can be evaluated by computing the (sample) mean of azimuth and elevation residuals across the batch, complemented by their respected standard deviations. These quantities are computed using the estimate from the last iteration of the LSQ (Equation (10)) $\delta\hat{\boldsymbol{\alpha}}_0^{\text{LSQ}}$, propagated analytically to each time stamp of the batch, mapped to the LoS and converted to azimuth and elevation via Equation (6). By comparing these predicted

DOI: 10.13009/EUCASS2025-555

angles ("PRED") to their ground truth counterparts ("TRUE"), the sample residuals are obtained, from which the mean and standard deviation are calculated as:

$$\mu_{\rho_\epsilon} = \frac{1}{|B|}\sum_{i=1}^{|B|}\left(\epsilon_i^{\text{PRED}} - \epsilon_i^{\text{TRUE}}\right) \tag{14}$$

$$\sigma_{\rho_\epsilon} = \sqrt{\frac{1}{|B|}\sum_{i=1}^{|B|}\left(\left(\epsilon_i^{\text{PRED}} - \epsilon_i^{\text{TRUE}}\right) - \mu_{\rho_\epsilon}\right)^2}. \tag{15}$$

Where $\epsilon = \eta, \psi$ and i indicates the element of the batch corresponding to the time instant t_i. These two quantities provide insight into the consistency and spread of the measurement fit; however, they may not capture convergence issues.[13] Particularly, if the filter settles around an incorrect local minimum, it leads to very low values of the these metrics but a erroneous estimate. To address this limitation, an additional metric is introduced based on state estimation accuracy. Specifically, the error in the estimated dimensional mean relative longitude ($a\delta\lambda$). As highlighted in the analysis conducted by Sullivan,[11] $a\delta\lambda$ is the weakly observable component of the ROE-state and when convergence is achieved in this component, all the other estimated elements of $\delta\hat{\boldsymbol{\alpha}}_0$ converge as well. Thus it is decided to use the estimation error on this quantity to evaluate the accuracy of estimation:

$$e_{\delta\hat{\lambda}} = a\delta\lambda_0^{\text{LSQ}} - a\delta\lambda_0^{\text{TRUE}}. \tag{16}$$

Where $a\delta\lambda_0^{\text{LSQ}}$ and $a\delta\lambda_0^{\text{TRUE}}$ are the second components of $a\delta\hat{\boldsymbol{\alpha}}_0^{\text{LSQ}}$ and $a\delta\boldsymbol{\alpha}_0^{\text{TRUE}}$, respectively. Together, these complementary metrics (μ_{ρ_ϵ}, σ_{ρ_ϵ} and $e_{\delta\hat{\lambda}}$) enable a comprehensive evaluation of the batch LSQ filter performance.

4. Results

In this work, all simulation scenarios share a common high-fidelity framework for ground-truth generation. At each time step, the simulator numerically integrates the inertial orbits of both spacecraft under a 30th-degree-and-order non-homogeneous Earth gravity field (GRACE dataset), including the effects of atmospheric drag (NRLMSISE-00 model), solar radiation pressure, and third-body perturbations from the Sun and Moon. The chief attitude is held fixed in the anti-flight direction.[14,22] Manoeuvres executed by the chief are introduced in the simulator as extended-time thrust burns (no execution error), whereas the deputy remains passive. Throughout each run, all relevant state (*e.g.*, $\boldsymbol{\alpha}_C(t)$, $a\delta\boldsymbol{\alpha}(t)$) and measurements quantities ($\eta(t)$, $\psi(t)$) are logged for subsequent evaluation of the performance metrics and to create batches of data for the filter. The spacecraft physical parameters are drawn from the PRISMA mission (see Table 3.5 of D'Amico[1]), and the chief initial orbit closely mirrors the Mango spacecraft orbit, as reported in Table 3. Test-specific details, such as relative orbit geometries, are described in their respective subsections.

Table 3: Initial mean absolute Orbital Elements of chief. Epoch: 2015-04-23 14:30:14

a [km]	e [-]	i [deg]	Ω [deg]	ω [deg]	M [deg]
7151.61	0.0016	98.52	355.89	11.05	28.98

4.1 Test 1: Propagation Accuracy

To conduct the test it is necessary to define the remaining variables needed to univocally define the simulation scenarios, namely the initial mean ROEs. Following the strategy explained employed in,[15] we define a family of initial relative orbits whose mean relative orbital elements are detailed in Table 4. The parameter c is sampled 10 times within the

Table 4: Initial mean ROEs

$a\delta a$ [m]	$a\delta\lambda$ [m]	$a\delta e_x$ [m]	$a\delta e_y$ [m]	$a\delta i_x$ [m]	$a\delta i_y$ [m]
0	0	c	0	c	0

range $[1, 30000]$ m in order to cover close range scenarios as well as mid and far ranges. For each sample a simulation is conducted with a time step of 10 s and a total duration of 10 (initial) chief orbit periods. No manoeuvre is conducted in this test, so the evolution of the motion follows the natural dynamics of the system. Notice that the relative orbit always remains bounded ($\delta a = 0$) and centred ($\delta\lambda = 0$). Moreover, it is shaped to have parallel relative eccentricity and inclination vector, in particular their x components is set to a non-zero value. This is deliberately chosen in order

DOI: 10.13009/EUCASS2025-555

to obtain a strong effect of J_2 on the relative motion, thus highlighting which model is capable of better capturing this perturbation. However, note that more challenging scenarios for models that do not properly account for geo-potential perturbations can be easily defined by introducing a mean along-track offset ($\delta\lambda \neq 0$), and even more so by introducing a drift ($\delta a \neq 0$).

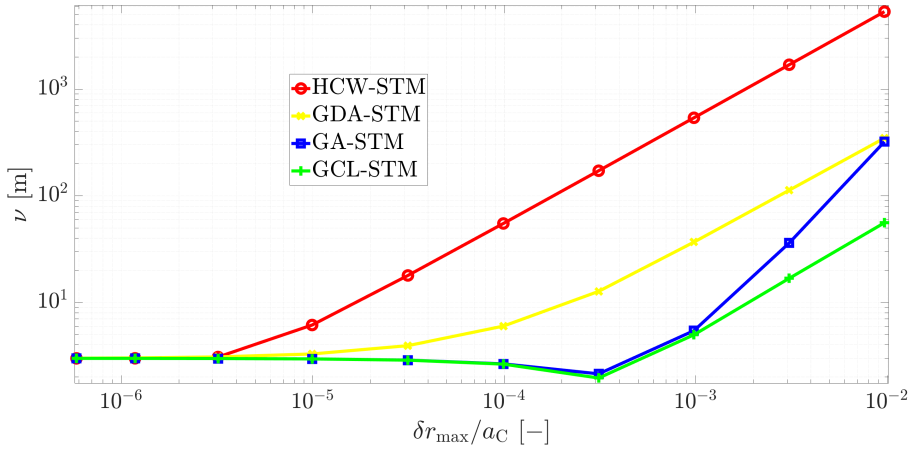

Figure 3: Propagation modelling error metric. Manoeuvre free case.

By sampling 10 different values of c in the specified range, the simulation is repeated for each initial ROE, the metric in Equation (11) is then evaluated once for each simulation scenario and plotted against the maximum distance achieved during the simulation. The results displayed in Figure 3 show that the importance of accounting for the geo-potential perturbation in the analytical propagation increases with the inter-satellite distance, confirming the analysis conducted in.[15] As the relative distance increases, using the advanced GCL-STM model (fully analytical) produces orders-of-magnitude better results than those obtained using the Keplerian one (HCW-STM) since GCL-STM considers the secular effects of J_2, J_4 and J_6 and improves the propagation via the second-order State Transition Tensor (STT) accounting for Keplerian and first-order J_2 as described in.[19]

4.2 Test 2: Manoeuvres Modelling

In this test the aim is instead to evaluate the (approximate) threshold burn-duration after which the assumption of impulsive manoeuvre has to be relaxed and whether the magnitude of the $\Delta\mathbf{v}$ influences this value. The evaluation metrics is the one described in Section 3.2 and a single initial relative orbit is used. Its parameters are reported in Table 5. In contrast to the family of relative orbits used for the unforced propagation accuracy test, this case introduces an along-track separation consistent with a far-range rendezvous scenario,[14] adding further generality to the analysis. To

Table 5: Initial mean ROEs

$a\delta a$ [m]	$a\delta\lambda$ [m]	$a\delta e_x$ [m]	$a\delta e_y$ [m]	$a\delta i_x$ [m]	$a\delta i_y$ [m]
0	−30000	400	0	−400	0

conduct the test, it is necessary to fix the number of manoeuvres and their magnitude and direction. In order to keep the analysis reasonably simple, a single manoeuvre is executed starting from simulation time $t_{\mathrm{M}}^{\mathrm{START}} = 100$ s. For the sake of generality, the direction of the manoeuvre is fixed along the unit vector $\mathbf{u}_{\Delta\mathbf{v}} = [1, 1, 1]/\sqrt{3}$, expressed in the RTN-frame. To evaluate the sensitivity to the magnitude of the manoeuvre, three values of $\Delta\mathbf{v}$ magnitude are selected: low $||\Delta\mathbf{v}|| = 0.001$ m/s, medium $||\Delta\mathbf{v}|| = 0.0055$ m/s and high $||\Delta\mathbf{v}|| = 0.01$ m/s. To understand when the assumption of impulsive burn is acceptable, we also need to define a range of Δt_{M} across which the $||\Delta\mathbf{v}||$ is spread. In particular, it is decided to distribute each value of $||\Delta\mathbf{v}||$ across 10 equally spaced burn-durations sampled from the time interval range: $\Delta t_{\mathrm{M}} \in [1, 5000]$ s. The manoeuvres are introduced in the simulator as distributed forces to generate the ground-truth, but the analytical propagation models described in Section 2 use either the single impulse or the set of equivalent impulses described in 2.2. Thus, in all simulations the motion of the chief is affected by a constant force:

$$^{R}\mathbf{f} = m_C \frac{||\Delta\mathbf{v}||}{\Delta t_{\mathrm{M}}} \mathbf{u}_{\Delta\mathbf{v}},$$

DOI: 10.13009/EUCASS2025-555

where m_C is the mass of the chief spacecraft. The constant force is applied from $t_{\mathrm{M}}^{\mathrm{START}} = 100$ s to $t_{\mathrm{M}}^{\mathrm{END}} = 100 + \Delta t_{\mathrm{M}}$ s to the CoM of the chief. A total of 30 sub-cases are simulated by combining the three manoeuvre magnitudes (low, medium, high) and 10 durations of the burns (ranging from 1 to 5000 s). The simulations are conducted with small time step of 0.1 s and a total duration of one (initial) chief orbit period, which lasts approximately 6000 s.

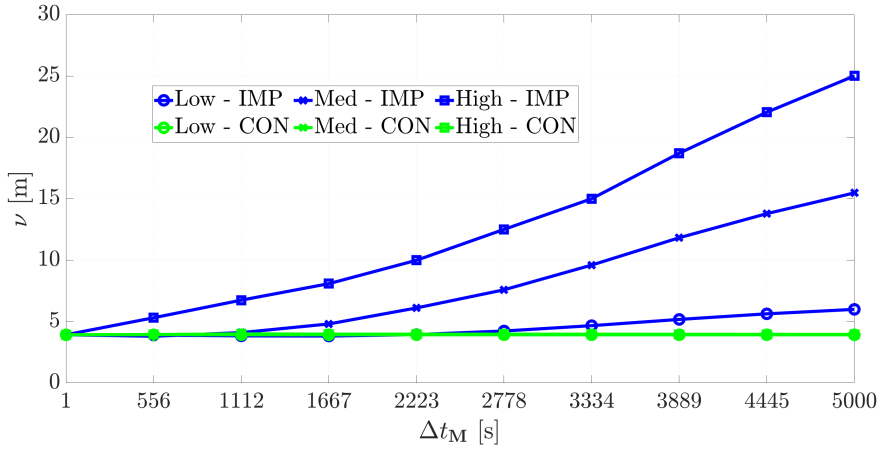

Figure 4: Propagation modelling error metric. Active manoeuvre case.

The output constitutes the ground-truth dataset. Consequently, the true initial orbit is re-propagated analytically (outside the simulator) using the GCL-STM model combined with first the single impulse assumption and then using the equivalent set of impulses to approximate a continuous manoeuvre. Finally, the metric of Equation (11) is computed and the results are displayed in Figure 4. The blue lines represent the cases where the analytical propagation is conducted using the impulsive assumption, while the green one assumes distributed manoeuvre modelled with an equivalent set of short impulses (1 s duration). The three green lines almost completely overlap and the propagation error metric ν remains constant with respect to both the burn-duration Δt_{M} and the magnitude level (low, medium, high). Indeed, a very fine discretisation of the originally continuous manoeuvre is expected to closely follow the ground-truth. Instead, when the single impulsive manoeuvre assumption is applied (blue lines), a dependency becomes apparent on both the duration of the burn and the magnitude of the manoeuvre. An increase in either factor make the assumption less realistic. However, the introduced error becomes significant only when $\Delta\mathbf{v} \geq 1$ cm/s and/or for burn durations lasting several minutes, suggesting that in many realistic scenarios, the assumption of single impulsive burn remains valid. A clear exception would be the case in which low-thrust propulsion is used. As a final consideration, it is important to note that the error metric is never exactly zero. This outcome is expected, as a residual error is present even in the absence of manoeuvres (see Figure 3). Moreover, the manoeuvre is applied to the mean orbital elements rather than the osculating ones, which introduces an additional source of error.

4.3 Test 3: Measurements Accuracy

This test goal is to determine which of the mapping of Table 2 most accurately computes the relative position vector ${}^{R}\delta\mathbf{r}$ starting from the ROEs. We proceed by defining a family of initial relative orbits. The parameter c is sampled

Table 6: Initial mean ROEs

$a\delta a$ [m]	$a\delta\lambda$ [m]	$a\delta e_x$ [m]	$a\delta e_y$ [m]	$a\delta i_x$ [m]	$a\delta i_y$ [m]
0	$-c$	$\frac{4}{300}c$	0	$-\frac{4}{300}c$	0

10 times within the range $[1, 30000]$ m in order to cover close range scenarios as well as mid and far ranges. The fractional parameter $4/300$ is selected so that the last sub-case coincide with the orbit defined in[14] as the starting point for the far-range rendezvous. For each sample a simulation is conducted with a time step of 10 s and a total duration of 10 (initial) chief orbit periods. No manoeuvre is executed in this test, so the evolution of the motion follows the natural dynamics of the system. These 10 cases constitute the ground truth. At this point, each of the LoS-models under analysis is used to map the ground-truth ROEs (and absolute mean OEs of chief) to ${}^{R}\delta\mathbf{r}^{\mathrm{MAP}}(t)$. By doing so for each time instant in each of the 10 sub-cases, the metrics in Equation (12) and (13) are computed. The results are reported in Figure 5. It is evident that the fully non-linear transformation GAC-MAP[22] significantly outperforms

DOI: 10.13009/EUCASS2025-555

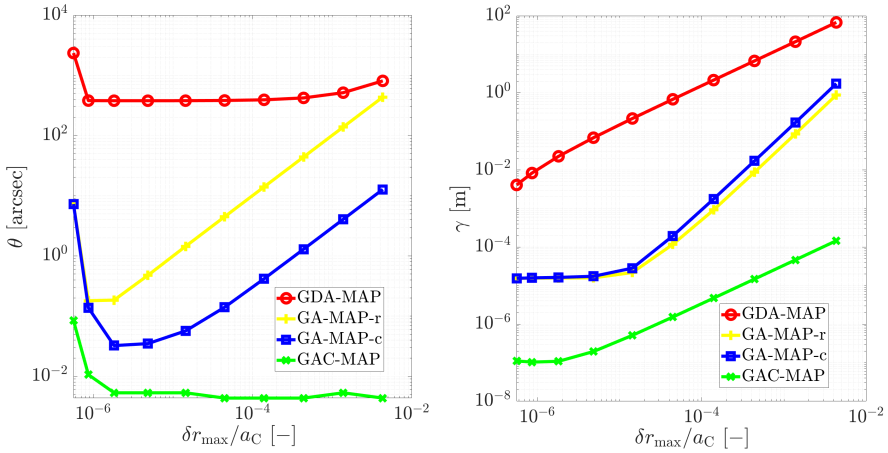

Figure 5: Line-of-sight modelling error metrics.

both the simple first-order linear mapping GDA-MAP employed in,[14] as well as the models derived from the Gim-Alfriend formulation[24] (GA-MAP). Notably, introducing the curvature correction (GA-MAP-c) yields a substantial improvement in angular accuracy, while the magnitude error remains largely unaffected. Interestingly, the angular error metric initially decreases with increasing inter-satellite distance for all LoS mappings. This trend may be attributed to the increasing separation between satellite causing the LoS to align with the $\hat{\mathbf{T}}$-axis. In contrast, the magnitude error exhibits a consistent and expected monotonic behaviour as a function of relative distance. It is also worth emphasising the several orders of magnitude difference in performance between the GAC-MAP model, whose maximum error remains within a fraction of a millimetre, and the other models, which can introduce errors up to 100 m.

4.4 Test 4: Estimation Accuracy

In this test the aim is to evaluate the influence of batch size and length on the estimation accuracy by means of the evaluation metrics introduced in Section 3.4. The ground-truth is generated by simulating the same relative orbit used in[14] (see Table 5) for a total of 10 chief (initial) orbits with a step of 0.1 s. No manoeuvre is applied in order to make the estimation process more challenging given the intrinsically weak observability of the problem. At this stage, no measurements noise is introduced in the observed quantities, thus the filter receives perfect measurements. Although unrealistic, it is still interesting to see how the filter behaves in the ideal noise-free scenario as the results can be used as benchmark for future analysis. To understand the sensitivity of the estimate to batch size and length, we proceed by sweeping combinations of these parameters which are used to slice the complete ground-truth dataset. The subset obtained from this batching process constitutes the batch of observations which is fed to the LSQ filter. The simplified process is sketched in Figure 1. In particular, 10 values of batch size $|B|$ are uniformly sampled from $[10, 1000]$ points and the same number of batch length Δt_B from $[10, 1000]$ min. Thus, a total of 100 different combinations (and batches) are constructed. For each of these batches, the LSQ algorithm described in Section 2.4 is run and the associated performance metrics are computed. In every case, the LSQ iterations are initialised using the same a priori estimate. The value of this estimate and its associated standard deviation are listed in Table 7. The accuracy of this estimate aligns with that typically achieved using Two-Line Elements, as also employed in.[8,14,19] Notice that, coherently to the greedy-approach used in this work, the LSQ uses the most accurate analytical propagation model (GCL-STM) and the most precise LoS mapping (GAC-MAP). The results are reported in Figure 6 and 7.

Table 7: A priori estimate and standard deviation of the initial mean ROEs.

	$a\delta a$ [m]	$a\delta\lambda$ [m]	$a\delta e_x$ [m]	$a\delta e_y$ [m]	$a\delta i_x$ [m]	$a\delta i_y$ [m]
$\delta\hat{\alpha}_0^{\text{APR}}$	8.3	−30478	438.1	17.7	−426.9	−311.5
σ_0^{APR}	20	1000	100	100	100	100

In both figures, the metrics are plotted against Δt_B and each curve correspond to a value of $|B|$. The residuals plots in Figure 6 show that regardless of the size of the batch, the LSQ filter can find a minimum. However, this does not imply that the LSQ iterations converge to the true value $a\delta\boldsymbol{\alpha}_0^{\text{TRUE}}$. The mean of the residuals is nearly zero for both azimuth and elevation, indicating that the estimate is unbiased. It is worth noting that if the LSQ solution had used the GA-MAP-r mapping without applying a curvature correction, a significant bias would appear in the azimuth. This

DOI: 10.13009/EUCASS2025-555

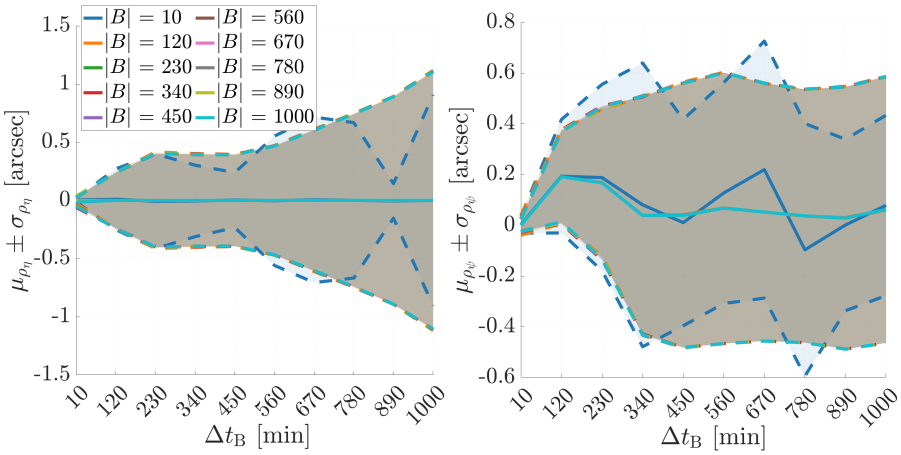

Figure 6: Mean and 1-σ bound of residuals: azimuth (left) and elevation (right).

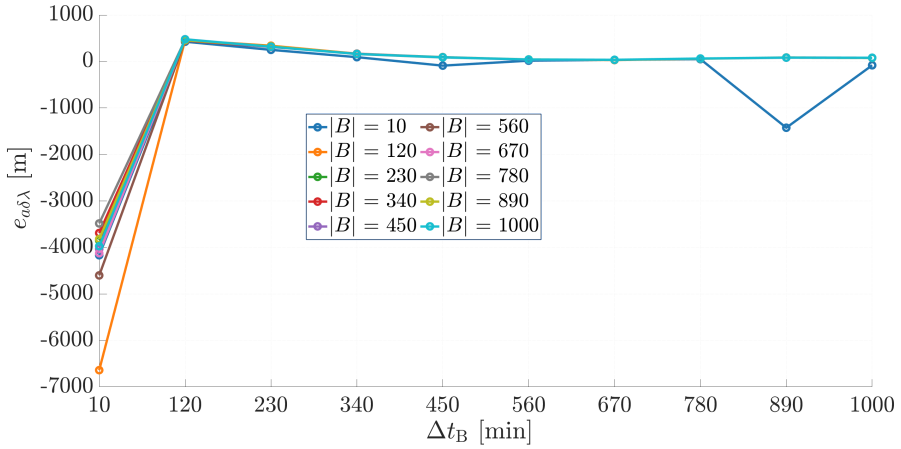

Figure 7: Initial mean relative longitude estimation error.

would result from an offset in the radial component of the relative state, caused by neglecting the orbital curvature. As the time interval Δt_B increases, so does the standard deviation, indicating that the estimation accuracy worsens a bit as we consider point further in the future. However, given the absence of noise, the residuals after the LSQ estimation process are almost irrelevant (order of magnitude of 1 arcsec). The risk of converging to an incorrect estimate is confirmed by Figure 7, where the error in the initial relative mean longitude reaches significant values when the batch length is shorter than 120 min. Specifically, the estimate shows a strong dependency on Δt_B for small batch lengths, which stabilises after approximately 600 s. While the sensitivity to the batch size $|B|$ is moderate for short Δt_B, it diminishes rapidly as the batch length increases. These results suggest that a small number of measurements may be sufficient to obtain an accurate estimate, provided they are well distributed along the relative orbit (see the right panel of Figure 2). On one hand, this is somewhat concerning, as in angles-only scenarios, measurements may be available only in specific orbital segments due to challenging illumination conditions.[8] On the other hand, it demonstrates that the analytical propagation model retains sufficient accuracy over longer time intervals. This opens the possibility of constructing a dataset with a small $|B|$ but extended Δt_B by using a few measurements acquired over different relative orbits. Furthermore, we show that only a limited number of data-points need to be stored and processed by the onboard LSQ filter, suggesting that an onboard implementation is indeed feasible.

5. Conclusions and Future Work

This work has presented a comprehensive sensitivity analysis of key modelling factors for angles-only relative orbit navigation within a batch least-squares framework. By systematically assessing the behaviour of propagation dynamics, manoeuvre modelling, line-of-sight mappings, and batch configuration parameters, we have identified optimal design options for each modelling sub-component, with the goal to maximise the overall performance achievable through

DOI: 10.13009/EUCASS2025-555

analytical implementation.

Firstly, the analysis confirms that employing a refined analytical propagation model (GCL-STM), which accounts for the geo-potential perturbations up to J_6 and includes second-order STT corrections, results in orders-of-magnitude improvements in propagation accuracy compared to the classical Keplerian (HCW-STM) model. Since GCL-STM is both precise and computationally efficient due to its analytical formulation, it is recommended as the preferred propagation model. Secondly, the study of manoeuvre modelling demonstrates that representing burns as impulsive events remains valid for typical Δv magnitudes up to approximately 1 cm/s and durations of a few minutes. For longer thrust arcs, this approximation introduces significant errors that grow with manoeuvre magnitude. In such cases, a continuous-thrust model, implemented for instance via discretisation into equivalent impulses, is necessary. A conservative threshold of 10 s is recommended, beyond which the impulsive assumption should be replaced. When employing the discretisation scheme described in Section 2.2, the same threshold should be used as the time step. Thirdly, the adoption of a fully non-linear LoS transformation (GAC-MAP) consistently yields sub-arcsecond angular accuracy and sub-millimetre magnitude error, significantly outperforming linear approximations such as GDP-MAP. Owing to its substantial accuracy improvement, the non-linear model is recommended, despite its slightly higher computational complexity. Finally, regarding the batch configuration, convergence of the least-squares solution is consistently achieved for batch lengths exceeding approximately 600 s, even with as few as 120 well-spaced measurements. Larger batches may be beneficial in mitigating measurement noise, which is not considered in the present analysis. Given the practical challenges in obtaining uninterrupted observation arcs of such length, primarily due to illumination constraints, it is advisable to design observation strategies that ensure coverage across the relative orbit. Since the employed propagation models remain accurate over multiple orbital periods, such coverage can be achieved by combining data points collected over successive revolutions, leveraging the natural variation in illumination induced by perturbation-driven orbital evolution or even accounting for it directly in the high level plan of the mission.

From an operational perspective, these findings represent a step toward enabling real-time on-board least-squares navigation, potentially offering both cross-verification and reinitialisation capabilities for sequential filters, thereby enhancing spacecraft autonomy. Moreover, the proposed methodology can be adapted for automated ground-based support, facilitating *post-facto* orbit determination. Future work will aim to extend this sensitivity analysis to account for measurement noise, operational constraints, and a broader range of mission scenarios.

6. Acknowledgments

This research is funded by Infinite Orbits SAS, grant reference UA.A.RRR.DAER.ELABS.AUTO.G8E4RICC00 PhD-GNC Rendezvous - RIF. 10/2024 GAIAS. The Authors would like to acknowledge GNC Engineer Daniel Opoka and GNC Engineer Raffaele Tarone for their support.

References

[1] Simone D'Amico. *Autonomous Formation Flying in Low Earth Orbit*. PhD thesis, Delft University of Technology, Delft, Netherlands, 2010.

[2] Simone D'Amico, Jean-Sébastien Ardaens, and Robin Larsson. Spaceborne autonomous formation-flying experiment on the prisma mission. *Journal of Guidance, Control, and Dynamics*, 35(3):834–850, 2012.

[3] Charity Weeden, Luc Riesbeck, Chris Blackerby, Nobu Okada, Eriko Yamamoto, Jason Forshaw, and John Auburn. Industry implementation of the long-term sustainability guidelines: An astroscale perspective. In *Proceedings of the 70th International Astronautical Congress (IAC 2019), 32nd IAA Symposium on Space Policy, Regulations and Economics*. International Astronautical Federation, 2019.

[4] Alessandro Scalvini, Alejandro Suarez, Saeed Rafee Nekoo, and Anibal Ollero. Finite-time state-dependent riccati equation regulation of anthropomorphic dual-arm space manipulator system in free-flying conditions. *Acta Astronautica*, 216:504–517, 2024.

[5] Alessandro Scalvini, Andrea Fois, Saeed Rafee Nekoo, Alejandro Suarez, and Anibal Ollero. Adaptive state-dependent riccati equation attitude control for rotation-flying dual-arm manipulators. In *Proceedings of the 2024 International Conference on Space Robotics (iSpaRo)*, pages 372–379, Luxembourg, 2024. IEEE.

[6] Svenja Woicke, Jimmy Jipp, Christian Steimle, Nils Pokrupa, and Lionel Metrailler. ADRIOS ClearSpace-1: In Orbit Demonstration of the Removal of a Non-Cooperative Spacecraft. In *Proceedings of the 9th European Conference on Space Debris*, pages 1–19, Bonn, Germany, April 2025. ESA Space Debris Office.

DOI: 10.13009/EUCASS2025-555

[7] Robin Biesbroek, Sarmad Aziz, Andrew Wolahan, Stefano Cipolla, Muriel Richard-Noca, and Luc Piguet. The clearspace-1 mission: Esa and clearspace team up to remove debris. In *Proceedings of the 8th European Conference on Space Debris*, pages 1–3. European Space Agency, 2021.

[8] Gabriella Gaias and Jean-Sébastien Ardaens. Flight demonstration of autonomous noncooperative rendezvous in low earth orbit. *Journal of Guidance, Control, and Dynamics*, 41(6):1337–1354, 2018.

[9] Simone D'Amico, Jean-Sébastien Ardaens, Gabriella Gaias, Heike Benninghoff, Benjamin Schlepp, and John L. Jørgensen. Noncooperative rendezvous using angles-only optical navigation: System design and flight results. *Journal of Guidance, Control, and Dynamics*, 36(6):1576–1595, 2013.

[10] Giuseppe Di Mauro, Margaret Lawn, and Riccardo Bevilacqua. Survey on guidance navigation and control requirements for spacecraft formation-flying missions. *Journal of Guidance, Control, and Dynamics*, 41(3):581–602, 2018.

[11] Joshua A. Sullivan. *Nonlinear Angles-Only Orbit Estimation for Autonomous Distributed Space Systems*. PhD thesis, Stanford University, 2020.

[12] Jean-Sébastien Ardaens and Gabriella Gaias. Flight demonstration of spaceborne real-time angles-only navigation to a noncooperative target in low earth orbit. *Acta Astronautica*, 153:367–382, 2018.

[13] Jean-Sébastien Ardaens. *Angles-Only Relative Navigation in Low Earth Orbit*. PhD thesis, Delft University of Technology, 2020.

[14] Gabriella Gaias, Simone D'Amico, and Jean-Sébastien Ardaens. Angles-only navigation to a noncooperative satellite using relative orbital elements. *Journal of Guidance, Control, and Dynamics*, 37(2):439–451, 2014.

[15] Joshua A. Sullivan, Sebastian Grimberg, and Simone D'Amico. Comprehensive survey and assessment of spacecraft relative motion dynamics models. *Journal of Guidance, Control, and Dynamics*, 40(8):1837–1859, 2017.

[16] David C. Woffinden and David K. Geller. Observability criteria for angles-only navigation. *IEEE Transactions on Aerospace and Electronic Systems*, 45(3):1194–1208, 2009.

[17] T. Alan Lovell and Taeyoung Lee. Nonlinear observability for relative satellite orbits with angles-only measurements. In *Proceedings of the 24th International Symposium on Space Flight Dynamics*, Laurel, Maryland, USA, 2014.

[18] Gabriella Gaias, Jean-Sébastien Ardaens, and Oliver Montenbruck. Model of j_2 perturbed satellite relative motion with time-varying differential drag. *Celestial Mechanics and Dynamical Astronomy*, 123(4):411–433, 2015.

[19] Gabriella Gaias, Camilla Colombo, and Martin Lara. Analytical framework for precise relative motion in low earth orbits. *Journal of Guidance, Control, and Dynamics*, 43(5):915–927, 2020.

[20] Adam W. Koenig, Tommaso Guffanti, and Simone D'Amico. New state transition matrices for spacecraft relative motion in perturbed orbits. *Journal of Guidance, Control, and Dynamics*, 40(7):1749–1768, 2017.

[21] Jean-Sébastien Ardaens and Gabriella Gaias. A numerical approach to the problem of angles-only initial relative orbit determination in low earth orbit. *Advances in Space Research*, 63(12):3884–3899, 2019.

[22] Gabriela Gaias, JeanSébastien Ardaens, and Camilla Colombo. Precise line-of-sight modelling for angles-only relative navigation. *Advances in Space Research*, 67(11):3515–3526, 2021.

[23] Oliver Montenbruck, Eberhard Gill, and F. H. Lutze. Satellite orbits: Models, methods, and applications. *Applied Mechanics Reviews*, 55(2):B27–B28, April 2002.

[24] Dong-Woo Gim and Kyle T. Alfriend. State transition matrix of relative motion for the perturbed noncircular reference orbit. *Journal of Guidance, Control, and Dynamics*, 26(6):956–971, 2003.

[25] Jonathan Grzymisch and Walter Fichter. Observability criteria and unobservable maneuvers for in-orbit bearings-only navigation. *Journal of Guidance, Control, and Dynamics*, 37(4):1250–1259, 2014.

[26] David A. Vallado. *Fundamentals of Astrodynamics and Applications*, volume 12 of *Space Technology Library*. Microcosm Press, 2 edition, 2001.